Environmental Science Nano

ROYAL SOCIETY OF CHEMISTRY

PAPER

View Article Online
View Journal | View Issue



Cite this: *Environ. Sci.: Nano*, 2025, 12, 433

# Multifunctional textured graphene-based coatings on elastomeric gloves for chemical protection†

Aidan Stone,[a] Zidan Yang,[a] Jiaman Wang,[a] Maria Louiza Dimtsoudi,[a] Aicha Sama,[a] Rebecca Martin-Welp,[a] Grey Small,[a] Indrek Kulaots,[a] Somnath Sengupta,[b] Francesco Fornasiero [c] and Robert H. Hurt *[a]

Received 6th July 2024,
Accepted 12th November 2024

DOI: 10.1039/d4en00601a

rsc.li/es-nano

Nanotechnology offers a variety of new tools for the design of next-generation personal protective equipment (PPE). One example is the use of two-dimensional materials as coatings that enhance the performance and ergonomics of elastomeric gloves designed to protect users from hazardous chemicals. Desirable features in such coatings may include molecular barrier function, liquid droplet repellency, stretchability for compatibility with the elastomer, breathability, and an ultrathin profile that preserves the user's manual dexterity and tactile sensation. The present work explores the potential of engineered graphene-based films with out-of-plane texturing as a novel platform to meet these multifold requirements. Graphene-based films in different formulations were fabricated from water-borne inks by vacuum filtration and solution casting methods on glove-derived nitrile rubber substrates. The various coatings were then subjected to tests of molecular permeation by model volatile organic compounds, droplet contact angle, breathability, and mechanical stability during stretching and solvent immersion. The films dramatically improve the barrier properties of glove-derived nitrile. The out-of-plane graphene texturing imparts stretchability through microscale folding/unfolding, while also enhancing droplet repellency in some cases through a lotus-like roughening effect. The combined results suggest that engineered textured graphene-based films are a promising platform for creating multifunctional coatings for a next generation of chemically protective gloves and other elastomer-based PPE.



### Environmental significance

The present work provides fundamental data that enable the rational design of personal protective equipment for use in environments containing hazardous chemicals. Ultrathin graphene-based coatings are formulated and applied to enhance the barrier properties of elastomeric gloves without seriously degrading user performance and ergonomics. This article also demonstrates methods to engineer the 2D coatings with out-of-plane micro-textures, binders and crosslinking agents to achieve the stability and stretchability required for practical exposure-prevention devices. The coating designs were also informed by the principles of green chemistry, and employ water-based inks, non-toxic polymer binders, and PFAS-free surface treatment agents to reduce the potential environmental impacts of device fabrication, use, and disposal.

## Introduction

Nanotechnology offers multifold opportunities for protecting human health by preventing exposure to hazardous substances. Emerging nanotechnologies are being developed for toxicant capture, removal, or degradation in water and air;[1–6] *in situ* remediation of contaminated soils,[7] and exposure prevention through nano-enhanced personal protective equipment (PPE).[8–13] Nanomaterials provide chemical protection by serving as catalysts,[14] molecular barriers,[10–11] sorbents,[9] or barrier/sorbent combinations in series.[13] The term PPE in chemical applications refers to a broad class of garments and wearable devices used to prevent contact between toxic or corrosive chemicals with the skin, eyes, or respiratory system. PPE are most often used in occupational settings, and may include overalls, aprons, footwear, gloves, glasses, face shields, respirators, or full suits.

The present work explores the potential of nanotechnology to enhance the performance and ergonomics of elastomer-based gloves for chemical protection. Chemically protective gloves are designed to prevent exposure through selection of appropriate materials of sufficient thickness to serve as

[a] *School of Engineering, Brown University, Providence, Rhode Island, 02912, USA. E-mail: Robert_Hurt@brown.edu*
[b] *Powerhouse Consulting Group, 9011 Chevrolet Drive, Suite 13, Ellicott City, MD 21042, USA*
[c] *Physical and Life Sciences, Lawrence Livermore National Laboratory, Livermore, California 94550, USA*

† Electronic supplementary information (ESI) available. See DOI: https://doi.org/10.1039/d4en00601a

molecular barriers. Work with highly toxic compounds often relies on thick butyl rubber gloves, but such thick protective layers impair tactile sensations, manual dexterity, and/or breathability.[8,9,15] It has been recommended to select the thinnest glove material compatible with protection from the specific chemical environment.[15] Here we explore the concept of using ultrathin, nano-enabled coatings on pre-formed thin gloves to enhance their barrier performance without significant loss of tactile sensation or "cutaneous sensibility"[16] and dexterity.

Among the various nanomaterial classes, two-dimensional (2D) forms show special promise in barrier applications due to their atomically thin, space-filling, sheet-like geometries. Much of the literature on 2D material barriers focuses on graphene, which in its ideal and pristine form blocks the transport of all atomic and molecular substances[17] and has been described as the "thinnest impermeable membrane".[18] Large-area graphene barrier technologies typically use graphene nanosheets (with micron-scale lateral dimension) rather than extended monolayers due to cost and processing advantages, and the nanosheets are assembled into randomly tiled multilayer films,[19,20] or imbedded as fillers in polymer matrices as barrier enhancers.[21] Some barrier applications use graphene oxide nanosheets,[13,19,22] which have enlarged interlayer spaces and serve as selective molecular barriers whose permeabilities are sensitive to molecular size and hydrophilicity[19,22] as well as solvent swelling effects on interlayer spacing.[23,24]

Elastomeric gloves are often stretched during use, but graphene coatings are not intrinsically stretchable and fail by cracking at low tensile strain. Recent work on graphene out-of-plane microtexturing[11,25–27] offers an approach to overcome this challenge by fabricating barrier coatings that mimic stretching through controlled folding/unfolding.[11] We hypothesize that thin (<150 μm) elastomeric gloves can be coated with ultrathin (<10 μm) textured graphene films that will improve chemical protection, accommodate normal stretching during use, and preserve much of the tactile sensation and dexterity associated with bare hand manipulation. While pursuing this hypothesis, we recognize that barrier coatings on gloves may also be asked to fulfill other requirements or functions for practical adoption. Fig. 1 shows a more complete set of seven target functionalities that may be required or desired depending on specific glove end use:

(i) Molecular barrier function – the ability to prevent permeation by a target chemical(s) in the case of vapor or direct liquid contact;

(ii) Dexterity and cutaneous sensibility – preservation of the user's ability to sense and manipulate objects with fine motor control;

(iii) Isotropic stretchability – the ability of a coating to accommodate the various stretching modes of the glove substrate during use without mechanical failure;

(iv) Solvent immersion stability – the ability to withstand full liquid immersion in water and other common solvents without softening or nanosheet shedding;

(v) Breathability – high water vapor transmission rates that allow the user to perspire with evaporation for thermal regulation and comfort;

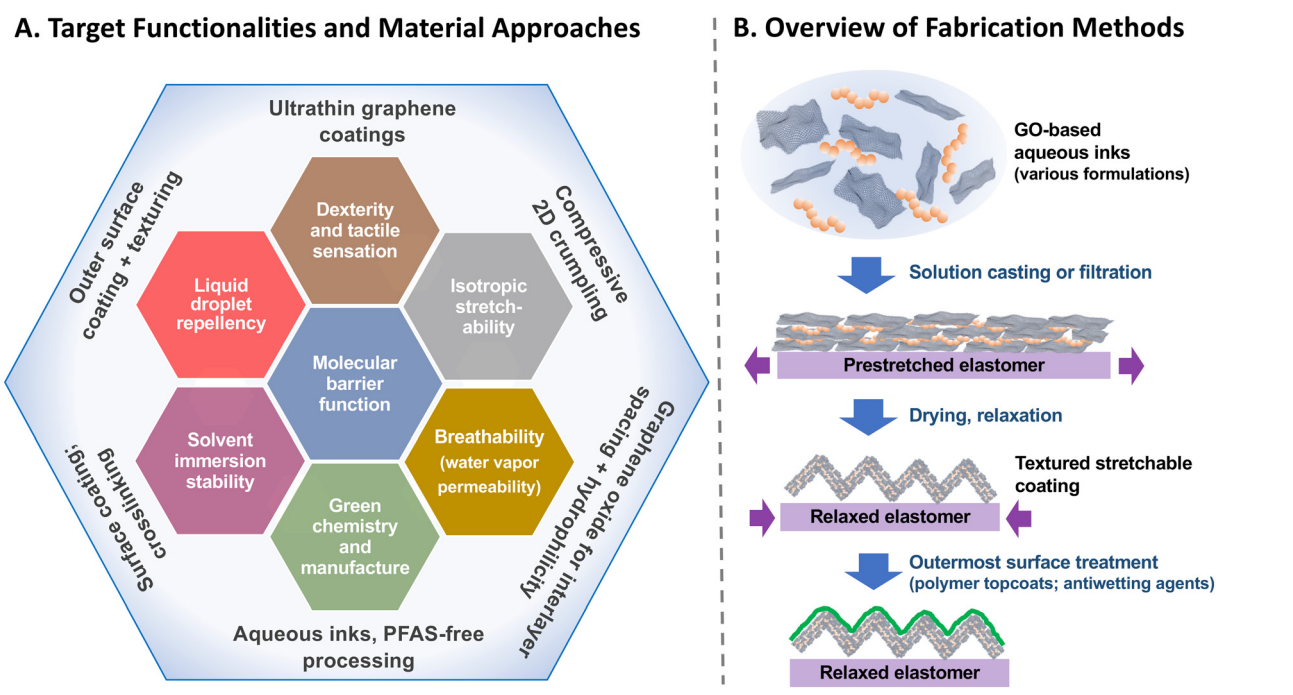


Fig. 1 Overall objectives and approach. A: Set of target properties for stretchable PPE coatings (hexagons), and the coating features and processing strategies used in the present study to address them (black text; outer rim). B: Overview of film fabrication steps and the corresponding material architectures.

 

(vi) Liquid droplet repellency – the ability to suppress liquid droplet wetting and spreading, which would lead to toxic chemical retention that increases the logistical burden of decontamination post-use. Ideally glove surfaces would be super-omniphobic, showing very high contact angles for a wide variety of liquid droplets. Note that this droplet repellency is a target functionality distinct from the molecular barrier function described in (i) above;

(vii) Green chemistry and manufacturing – desirable features include the use of non-toxic polymer binders, water-based ink formulations for coating deposition, and the absence of polyfluoroalkyl substances (PFAS) and other fluorochemicals in processing.

It is challenging to develop a single material system that can simultaneously exhibit each of these target functionalities. However, 2D textured graphene oxide films are known to possess some of these features barrier properties,[11,19,28] water processibility, breathability,[19,28] isotropic stretchability[11,25,26] and can possibly be engineered or enhanced to address the other three. The goal of this work is to explore how textured GO films can be used as a platform to create and evaluate coating formulations that address each of the various features desired in PPE. Fig. 1A shows the materials approaches taken to address each desired functionality in turn, and panel B demonstrates the typical fabrication steps employed here. The data presented will provide guidance for the design and fabrication of graphene-based glove coatings that can be tailored for different challenges in chemical protection.

# Experimental

## Materials

Methyl cellulose (MC) powder (4000 cP 2% in water), polyallylamine hydrochloride (PAA) (50 000 $M_w$), glutaraldehyde solution (grade II, 25% in water), L-ascorbic acid (99%), carboxymethyl cellulose salt (medium viscosity in water), branched polyethylenimine (800 $M_w$), and commercial grade *N*-(3-dimethylaminopropyl)-*N*′-ethylcarbodiimide hydrochloride (EDAC) were purchased from Sigma Aldrich. Citric acid monohydrate was purchased from Fisher Chemical. Styrene butadiene rubbers were purchased from Mallard Creek Polymers (Charlotte, NC). Carbodiimide crosslinkers were purchased from Stahl (Waalwijk, Netherlands). The polyurethane dispersion was from Synthetic Natural Polymers (SNP) (Durham, NC). The epoxy ester dispersion was bought from Allnex. Plastidip (Plastidip in Blaine, MN), Ames Blue Max (Ames Research Laboratories in Salem, OR), and Flexseal (Swift Response in Weston, FL) were purchased retail. All solutions were prepared using deionized water. Selected films were treated with commercial PFAS-free antiwetting sprays. Nanoman fabric waterproofing spray (Nanoman, Notting Hill, Victoria, Australia) is a silica-based, PFAS free, VOC-free breathable formulation for indoor use. DetraPel outdoor fabric protector (DetraPel, Framingham, MA) is advertised as breathable and fluorochemical free. ProtectMe premium fabric protector (ProtectMe, Melbourne, Australia) is a silica-based, PFAS free spray agent. Each product was applied and then dried per manufacture recommendations.

## Graphene oxide synthesis and film assembly

Graphene oxide was synthesized and purified in-house using a modified Hummers' method following the procedure in Spitz *et al.*[19] and used in previous studies[11,29,30] – (see ESI†). Monolayer GO nanosheets of nominal 1 μm (lateral dimension) were harvested into aqueous stock suspensions of 1–3 mg ml$^{-1}$. Thermally reduced GO (rGO) free-standing films as a reference material for FTIR were prepared as explained in our earlier work.[31] Films were produced from a series of graphene-based inks prepared to have equal GO concentration (0.5 mg ml$^{-1}$). Composite inks based on GO/methylcellulose/glutaraldehyde (GO–MC–GA) were formulated by adding powdered MC polymer and GA crosslinker to a diluted GO stock, to give an ink concentration of 0.5 mg ml$^{-1}$ (GO); 2 mg ml$^{-1}$ (MC); and 1 mg ml$^{-1}$ (GA). The solutions were stirred at room temperature for 24 hours then homogenized by bath sonication for 10 min.

Multilayer nanosheet films were prepared from the inks by two methods: vacuum filtration on porous filters and solution casting on fully dense elastomer substrates. The vacuum filtration method used 20 ml of graphene-based ink charged to a 300 ml, 47 mm diameter glass Buchner funnel on a vacuum-pumped Erlenmeyer flask with Durapore porous PVDF membrane filters with pore sizes of 0.45 μm. The resulting films have a nominal thickness of 3 μm (for pure GO films) or 10 μm (for GO–MC–GA films). The films were used either in a freestanding state (after removal from the filter) or supported on the highly porous PVDF filter substrates (70% porosity) that offer no significant mass transfer resistance in permeation testing. The solution casting method was used to create coated elastomers for wrinkling and stretching experiments, and to simulate scalable spray and dip coating processes. The solution casting technique involves pipetting 2 ml of ink onto elastomeric substrates (150 μm thick nitrile films cut from the palm region of Kimberly Clark powder-free purple nitrile exam gloves, model KC500) within a film area defined by a 4 cm diameter metallic ring that confines the liquid pool (Fig. S1†). The nitrile substrates were pre-treated in oxygen plasma (20 min in 500 mTorr air) to enhance water wetting and spreading. Film thicknesses were 0.5 μm (pure GO) and 5 μm for GO–MC–GA composite films. Both types of films were air dried at room temperature for at least 24 hours prior to use, and selected films were further dried in a 60 °C oven.

Textured (wrinkled/led) films were fabricated by biaxial mechanical compression methods adapted from prior studies.[11,27,32] Whole nitrile gloves ($O_2$ plasma pre-treated) were pre-stretched by either (i) compressed-air inflation,[11] or (ii) mechanical stretching and clamping[27] induced by insertion of a 10 cm-diameter aluminum disk into the glove interior. Most experiments used the aluminum frame

method, which produced a more uniform and planar biaxially stretched elastomer patch on the disk face, which was then clamped in place and trimmed to size (Fig. S2†). Four points in a rectangle were marked and measured prior to stretching and re-measured after stretching to determine the strain and ensure strain uniformity in both $X$ and $Y$ dimensions. Then, 2 ml of GO-based ink were pipetted into the confining ring and room-air dried (typically) or oven dried. Finally, the graphene-coated elastomer cut-outs were removed from the frame to undergo relaxation that causes graphene film biaxial compression and thus out-of-plane film deformation (texturing). To create imbedded (sandwich) architectures, graphene-based films were first assembled on nitrile substrates and dried (as above), then overcoated with commercial polymer-based topcoats (Plastidip spray coating; FlexSeal dip/pour coating diluted to 50 wt% in hexane), which are premixed with any relevant crosslinking/curing agent (see Tables S1 and S2†), and air-dried for 48 hours.

### Characterization

The surface and cross-sectional morphologies of the planar, imbedded, and wrinkled GO films were imaged by a Thermo Scientific Quattro S Environmental Scanning Electron Microscope (SEM) operating at 10.0 kV. The sandwich architectures were characterized by optical microscopy with fiber optic back-lighting to reveal the internal graphene-based film structure. Thermogravimetric analysis was performed with a Mettler Toledo TGA/DSC-1 Star system. The sample heats of decomposition and vaporization were measured by the Q20 model Thermal Analysis (TA) Instruments – Waters LLC Differential Scanning Calorimeter (DSC). FTIR spectra were collected with the Jasco Instruments FT/IR-4100 with an Attenuated Total Reflectance (ATR) accessory. A Thermo Fisher Scientific K-Alpha X-ray Photoelectron Spectrometer (XPS) was used to obtain the XPS spectra from which atomic C/O ratios were calculated. The $N_2$ (at 77 K) and $CO_2$ (at 273 K) vapor adsorption isotherms were measured with an Anton-Paar (formerly Quantachrome) Autosorb-1. All films and powder samples were outgassed at 80 °C for 48 hours to ensure that the sample surface for the gas adsorption experiments is clean. The surface areas were calculated by applying the Brunauer–Emmett–Teller (BET) model.

### Permeation studies

The graphene-based films were characterized for water vapor transmission rate (WVTR) using both a static method[29] (Fig. S3†) and a dynamic method[33–35] (Fig. S4†). In the static method, 150 ml liquid water is added to a two-piece O-ring sealed glass vessel of 200 ml. The test film was supported on a PVDF membrane and epoxy-glued over a 2 cm diameter hole on an aluminum plate. Water in the glass vessel was preheated to 60 °C and then an aluminum plate with the test film was clamped onto the glass vessel and sealed with the O-rings. The total mass of the setup was recorded and then the sealed vessel was placed in a 60 °C oven for 6 hours. Water vapor permeation was calculated by gravimetric loss and corrected to the standard conditions (37 °C and a driving force of 90% relative humidity difference). Permeation rates were also measured for hexane as a model non-polar volatile organic compound, and the $n$-hexane permeation experiments followed the same procedure above but were conducted at room temperature for 24 hours using 35 ml liquid hexane in a 45 ml vessel.

Fig. S4† shows the dynamic moisture permeation cell,[33] which was used with a previously developed method.[34,35] Briefly (Fig. S4†), both sides of the films were exposed to 1000 sccm $N_2$ gas streams with controlled relative humidity (RH) to establish a 50% RH difference across the sample. To ensure that all measured transport is driven by a concentration gradient, the pressure differential across the membrane (monitored by an Omega PX409-001DWUI differential pressure transmitters) was set to zero with a back-pressure regulator. After the system reached steady state, the difference between the measured RHs of the incoming and outgoing gas streams (monitored by two Vaisala HM70 RH sensors) at the back side of the GO films was used to calculate the mass flow rate ($m$) of water vapor diffusing across the film, according to the relation $m = Q \times \Delta C$, where $\Delta C$ is the difference between the two gas stream water concentrations and $Q$ is the total flow rate (1000 sccm). To determine the potential dependence of water vapor permeability on the material hydration level, the breathability assessment of the of GO membrane composites was performed at 30 °C and at two mean RH (30% and 50%), here defined as the RH average of the two incoming gas streams. The temperature was controlled with a thermostated box encasing the DMPC cell.

To quantify the permeation of diethyl chlorophosphate (DCP) through 2D membranes, a custom-built, temperature-controlled permeation system was used hosting a Teflon AVLAG (Aerosol Vapor Liquid Assessment Group) cell and in-line GC-FID sensors. The permeation measurements were made by established methods.[33] Specifically, the membrane was placed into a diffusion cell having a gas inlet and outlet in the base semicell. For vapor contact experiments, a Kimwipe film was used to wick and spread evenly a 1 μL droplet of DCP above the test membrane to ensure that the membrane surface is uniformly exposed to DCP vapor. The top semicell was then sealed with a Teflon cap equipped with o-rings, so that the stagnant headspace above the sample surface became saturated with the evaporated DCP. A high purity dry $N_2$ sweep (60 $cm^3$ $min^{-1}$) below the sample was used to carry any permeated DCP to a flame ionization detector (SRI Instruments, gas chromatograph model 8610C). Before each experiment, the FID signal was recorded in the absence of any chemical until a stable baseline was achieved. During a test run, if permeation occurred, data was collected for many hours (12–16 h) until the FID signal returned to the baseline level. For impermeable films, the permeation experiment was terminated after a shorter collections time

 

(at least 3 h). Permeation data reported here were baseline corrected and time shifted so that time zero corresponds to the time of DCP injection into the cell top chamber.

Liquid simulant permeation was quantified with the same set-up employed for DCP vapor and a slightly modified procedure. Here liquid DCP (20 μl) was placed in direct contact with the entire permeation area of the 2D test membrane (~1 $cm^2$), which was defined by the rim of glue (EP41S-5 solvent resistant epoxy, MasterBond) used to attach the 2D sample to the supporting Kapton film. The chosen amount of DCP was sufficient to form a pool of liquid covering the membrane sample. As for vapor testing, a 60 $cm^3$ $min^{-1}$ dry $N_2$ sweep carried the permeated simulant to an in-line FID. The PeakSimple chromatography software (SRI Instruments) was used to record any FID signal deviation from a stable baseline obtained just before the DCP experiment with a pure $N_2$ gas stream. Permeation data reported here were baseline corrected and time shifted so that time zero corresponds to the time of DCP injection into the cell top chamber.

### Stretchability experiments

Selected films were characterized for stretchability as needed for some wearable textile or elastomer applications. Films were prepared with different pre-stretch linear strains, $\varepsilon$, defined as:

$$\varepsilon = \frac{d_{\text{stretched}} - d_{\text{original}}}{d_{\text{original}}} \times 100\% \quad (1)$$

where $d_{\text{original}}$ is the distance between two adjacent marked points in the relaxed state and $d_{\text{stretched}}$ is the distance after stretching. Pre-strains of 33%, 50%, 66%, 83% and 100% were used, and films were deposited, dried, and relaxed, then gradually re-stretched under a stereomicroscope or digital camera to identify the critical strain for failure, and to observe the nature of the cracks at the failure point. Failure was characterized by measuring crack density (sum of all crack widths per unit area of microscope image) as a function of strain.

### Liquid droplet wetting experiments

The interaction of planar and textured GO films with sessile liquid droplets was characterized using a horizontally mounted low-power optical microscope (Zeiss Stemi 2000-C) outfitted with digital camera (Canon DS126481) and fiber optic lighting. A goniometer (Rame-hart CA 190-U1) was used for droplets with low contact angles (<40°) the contact angles extracted by DROPimage Advanced. Selected films were treated with antiwetting spray coatings (see Materials) and left to dry in air for 24 h. Five μL droplets of water or diethyl malonate (nerve agent simulant) were pipetted onto the surface and the digital images were analyzed using a contact angle plugin in Image J. Reported contact angles are averages of about 5 droplets on two different samples of each film type.

## Results and discussion

### Screening of graphene ink formulations

Existing literature suggests that pure graphene oxide films fulfill some of the target functions for practical PPE coatings, including barrier properties to organic compounds[18,19] breathability.[19,28] However, pure GO films are not sufficiently stable under direct contact with polar liquids (target functionality iv), which can lead to softening and/or nanosheet shedding or redispersion.[36] Here we address the solvent stability challenge through addition of polymeric binders with crosslinking, while retaining high GO loadings to maximize barrier performance. As an alternative we explore polymer topcoats that prevent direct water contact with pure GO films. Because we target water-based green manufacturing, we focus effort (i) on aqueous ink formulations that incorporate GO and waterborne polymer binders, and crosslinking to stabilize those polymers for direct contact with liquid water or other polar solvents during use. Guided by the literature on graphene–polymer composites and crosslinking,[10,12,21,37–43] we selected and screened 18 binder, crosslinker, and topcoat formulations to identify robust, water-processible, yet liquid-water stable composite films (ESI† Tables S1 and S2).

A promising binder/crosslinker combination from this screening study was methylcellulose (MC) as binder[37,40,44] and glutaraldehyde (GA) as crosslinker (see Fig. 2). Methyl cellulose is a non-toxic, non-allergenic, water-processible synthetic polymer used in food and consumer products and as a binder in pharmaceutical formulations. Glutaraldehyde is commonly incorporated as a stabilizer for biomaterials, specifically as a crosslinker for proteins. The MC–GA system has been used previously to fabricate graphene-enabled gas barriers and membranes[37,40,44] but prior studies do not address stability of GO toward polar solvents nor use high-GO-loading, nacre-like formulations on elastomers.

### Characterization

Fig. 3 and 4 and S5–S8† provide structural, chemical, and physical characterization of the graphene-based films. The planar films made by solution casting on plasma-pretreated nitrile develop subtle topographical contours during fast oven drying, which are visible by the naked eye, and for the imbedded films with topcoats are visible under fiber optic backlighting (Fig. 3A and S6†). Slower drying in room air reduces these contours and improves planarity. The pre-stretch/deposition/relaxation sequence produces textured GO films with complex crumple features of 10–30 μm length scale (Fig. 3B and C). Both the glove inflation method and the mechanical frame stretching method successfully introduce the desired out-of-plane textures (Fig. S7†). Larger pre-strains create finer scale features (compare 85% to 66% pre-strain in Fig. S7†), which is a trend also reported previously.[27] XRD analysis shows a strong GO peak corresponding to an interlayer spacing of 0.91 nm, and this peak disappears in the composite (Fig. 3D). Cross-sectional

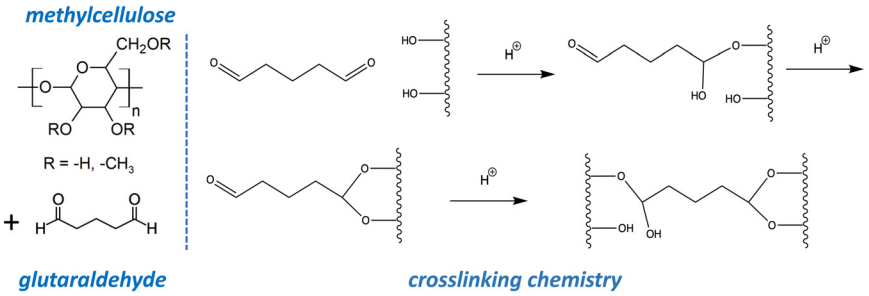


Fig. 2 Molecular structures and crosslinking mechanism relevant to the GO–MC–GA composite coatings. Glutaraldehyde is reported to be effective as a crosslinker of hydroxyl groups,[45–47] and the mechanism is initiated by nucleophilic attack by hydroxyl oxygen on the carbonyl carbons, resulting in glutaraldehyde fixation to polymer and/or GO by ether linkages.

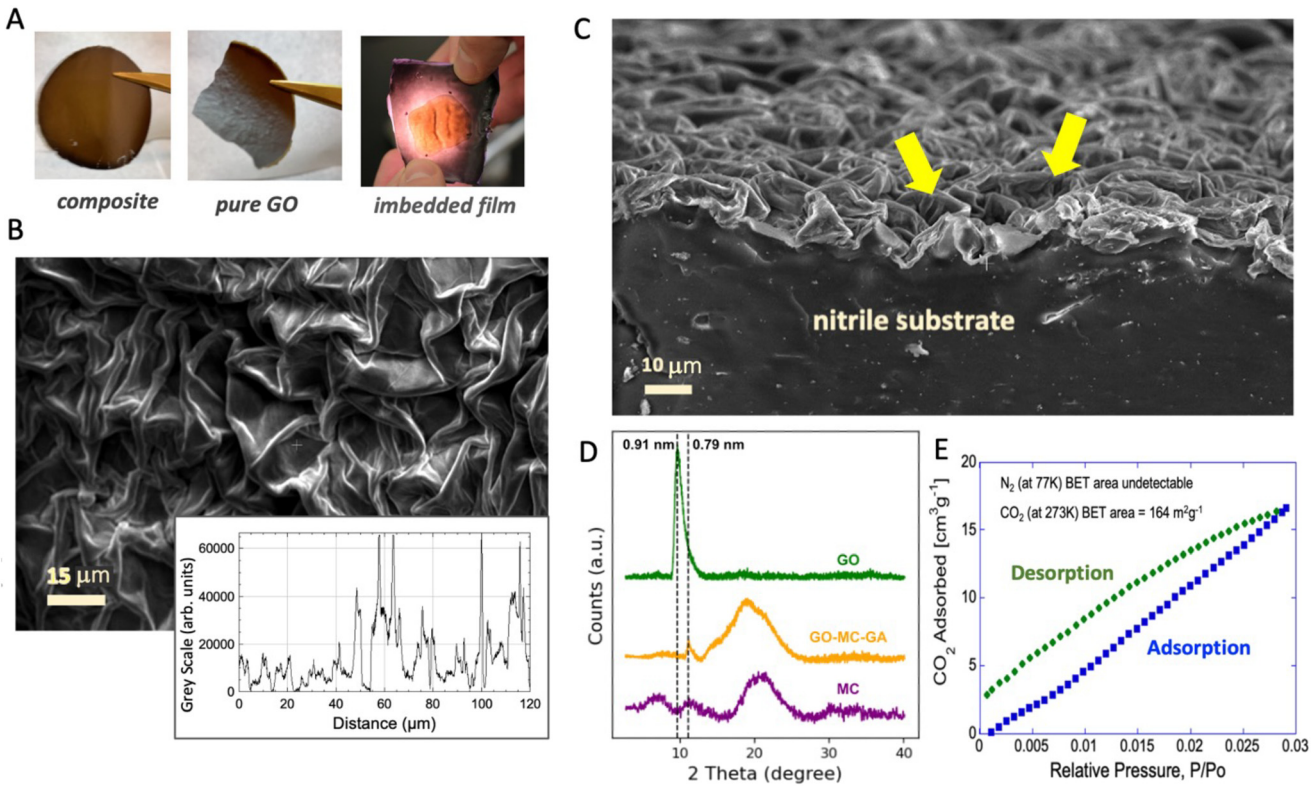


Fig. 3 Structural characterization of graphene-based films. A: Photos of pure, composite and imbedded GO films. The composite films are noticeably less flexible (have higher bending stiffness) than pure GO films. B: Textured GO films fabricated by the mechanical stretch method at 66% isotropic pre-stretch. Inset is a grey-scale line profile showing a ~10 μm wavelength scale for the primary out-of-plane textural features. C: Cross-sectional view of a textured GO film (66% pre-stretch) after freeze fracture using tilt-stage SEM (yellow arrows show example complex, 3D cavities). D: XRD spectra for pure GO, the composite, and pure methyl cellulose, showing the interlayer spacing in pure GO films (0.91 nm), and its absence in the GO–MC–GA composite, indicating the loss of nanosheet when the polymer is introduced. E: Vapor adsorption isotherms and computed internal surface areas for the GO–MC–GA film.

images of these films show a strongly aligned microstructure parallel to the substrate (Fig. S5†), so the lack of an XRD peak for the interlayer spacing suggests that the polymer (methylcellulose) is interleaved with the nanosheets and suppresses the nanosheet stacking that leads to the characteristic spacing in pure films.

Vapor adsorption experiments reveal measurable uptake of $CO_2$ at 273 K by the MC–GO–GA composite film (panel E), which corresponds to 164 $m^2$ $g^{-1}$ internal surface area by the BET theory. The surface area based on $N_2$ uptake at 77 K is much lower (undetectable due to low film mass and instrument limitations). This $CO_2/N_2$ difference is seen in other carbon material systems and is widely interpreted as an indication of molecular-sized pores (0.8 nm and below), in which $N_2$ diffusion is activated and thus slow at the standard $N_2$ measurement temperature of 77 K.[31] The composite film $CO_2$ surface areas are 4-fold larger than those for pure GO and rGO films (maximum 40 $m^2$ $g^{-1}$, see Kwon *et al.*[32]),

 

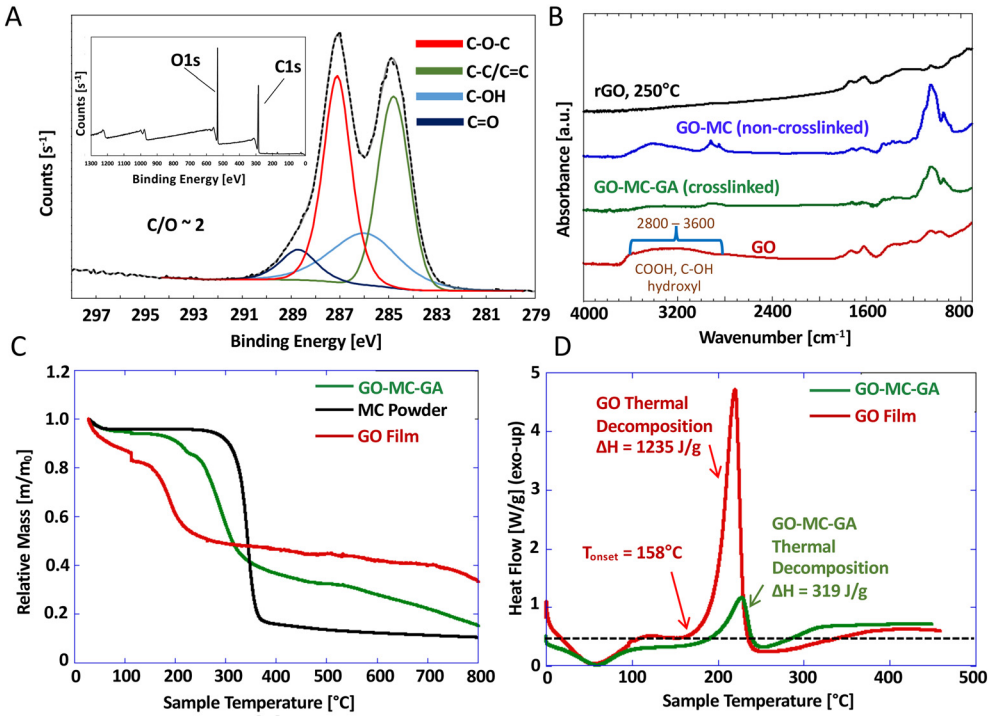


**Fig. 4** Spectroscopic and thermal characterization of pure GO and composite films. A: XPS characterization of GO films: C1s high-resolution spectrum with peak deconvolution and survey spectrum inset. B: FTIR spectra of GO films, crosslinked (GO–MC–GA) and non-crosslinked (GO–MC) films, and rGO films (thermally reduced) as a reference. C: Thermal gravimetric analysis traces showing the decomposition behavior of the composite compared to pure GO and MC. D: Differential scanning calorimetry traces showing the characteristic exotherm of GO thermal decomposition in both the pure GO and GO–MC–GA composite films.

possibly reflecting pores formed by the interruption of regular sheet stacking by the polymer binder.

Fig. 4 shows spectroscopic and thermal characterization of the graphene-based films. The XPS survey spectrum (Fig. 4A inset) gives a C/O atomic ratio of 2.1, which is typical of Hummers-synthesized GO.[19,32] The high-resolution C1s spectrum (Fig. 4A) is deconvoluted to give a typical speciation pattern, and the full oxygen 1s spectra is shown in Fig. S8.† Fig. 4B shows FTIR spectra that provide support for the hydroxyl crosslinking mechanism of Fig. 2. There is a significant decrease in hydroxyl functional groups in GO after the addition of MC and GA, as seen by the absence of a broad peak between 2800–3600 $cm^{-1}$. This peak is also absent in the rGO film (thermally reduced at 250 °C), which also shows a significant reduction of the peak between 900–1100 $cm^{-1}$ (corresponding to various C–O bonds). The GO–MC–GA film synthesis occurs at room temperature, so the loss of features from 2800–3600 $cm^{-1}$ are not due to thermal reduction, but likely to formation of new bonds through GA-mediated crosslinking of hydroxyl groups of GO and MC. More intense C–O features were observed in GO–MC–GA films relative to those for unmodified GO and rGO, which could be attributed to the formation of new acetal linkages and/or the introduction of ether groups from MC.

The non-crosslinked GO–MC film shows a sharp 900–1100 $cm^{-1}$ peak, demonstrating the presence of polymer ether bonds like those of the crosslinked GO–MC–GA structure. The non-crosslinked spectrum also presents a broad peak between 3000–3600 $cm^{-1}$, indicating the presence of hydroxyl groups that are notably absent within the crosslinked version of the composite film, providing further evidence that glutaraldehyde crosslinking involves bond formation between the hydroxyl moieties of polymer and of GO.

TGA spectra in Fig. 4C show the GO composite decomposes first (with an onset ~200 °C) before the polymer (onset ~300 °C). The presence of the polymer slightly increases the thermal stability of the GO component relative to pure nanosheet films (decomposition onset ~150 °C). DSC measurements on crosslinked GO–MC composite films (Fig. 4D) show a marked decrease in heat of decomposition compared to unmodified GO ($-\Delta H$ = 319 J $g^{-1}$ and 1235 J $g^{-1}$, respectively). The composite data confirms the exothermic decomposition characteristic of GO, but it is reduced in magnitude by a factor similar to the GO mass fraction in the composite (25%).

## Molecular barrier function

Molecular permeation through GO/rGO films and composites has been well studied[19,20,22,28,48–51] due to its importance in separation membranes and barrier films. For the present class of application, the films were characterized for permeation by volatile organic compounds (VOCs) using

*n*-hexane ($C_6H_{14}$, B.P. 69 °C, minimum projected diameter: 0.28 nm,[52] hydrophobicity: log *P* = 3.9) as a model VOC in a batch gravimetric permeation cell. Then selected films were tested in more detail for permeation by the nerve agent simulant, diethyl chlorophosphate, DCP ($C_4H_{10}ClO_3P$, B.P. 60 °C, equivalent spherical diameter 0.78 nm, hydrophobicity: log *P* = 1), in a dynamic flow device.

Fig. 5 shows hexane results as vapor permeation rates under standard conditions (20 °C, saturated vapor). The GO–MC–GA composite films, both as-produced and oven dried, have hexane permeabilities below the detection limit, and about 200× below the positive control (a porous PVDF filter used as film backing). In contrast, the pure GO films have hexane permeabilities that depend on processing history. Films that were oven dried at 60 °C for 5 h or 48 h post-synthesis showed permeation below the detection limit, while films subjected to no thermal drying operation (only 24 h in room air after synthesis, labeled "present study") have hexane permeabilities >1000 g $m^{-2}$ per day. Hydrated GO nanosheet films have been reported to show increased interlayer spacing[23,24,53] and permeability.[49] Thermal drying after synthesis appears to improve barrier performance, and the effect persists to some extent even after subsequent immersion in liquid water (Fig. 5). The composite films are better barriers than pure GO against hexane vapor in both the dry and partially hydrated states.

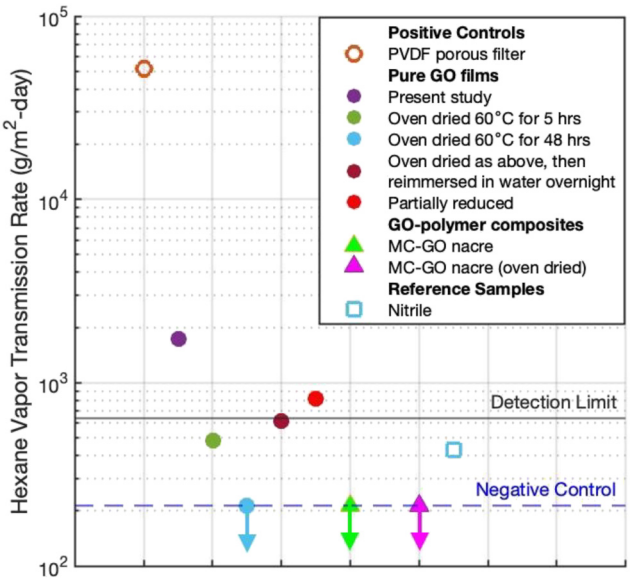


**Fig. 5** Experimental hexane vapor transmission rates of pure GO films and GO–MC–GA composite films measured by a gravimetric permeation method. The *Y*-axis shows the flux from a saturated vapor from a liquid hexane source at 20 °C to the room air above the film. Test films are supported on a porous PVDF membrane of negligible diffusional resistance (see positive control for PVDF filter). Negative control samples are measured with a metal foil barrier. The lower detection limit is set at 3× the negative control value. Dry GO films and the GO–MC–GA composite are at or below the negative control value. The standard errors are on average ± 5% for samples far above the detection limit.

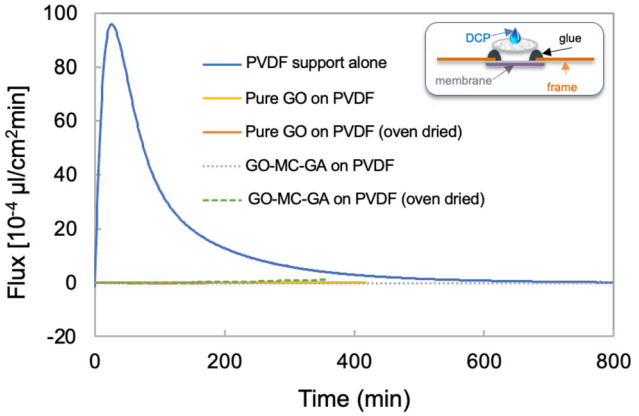


**Fig. 6** Diethyl chlorophosphate (DCP) permeation rates through GO (3 μm) and GO–MC–GA (10 μm) films under conditions of vapor-only contact. All films are supported on a porous PVDF filter during testing, which allows rapid DCP vapor permeation when used alone as a positive control. All films studied here are effective DCP vapor barriers.

Fig. 6 and 7 and S9† show results of dynamic permeation experiments with DCP. Here a fixed amount of DCP is introduced to the device and exposed to the test films by either vapor or liquid contact (see sketches in Fig. 6 and 7), and any permeant is collected from the backside in a flowing carrier gas. The results are presented as time profiles of DCP flux until the droplet is depleted. In the vapor-only contact mode (Fig. 6), the liquid droplet is capillary infiltrated into a cloth suspended just above the test film (see inset). All graphene-based films tested in this contact mode were effective barriers for DCP vapor, giving flux values below the detection limit (Fig. 6). Note the PVDF backing that supports the tests films has a very low resistance to DCP vapor permeation (blue curve), so the good vapor barrier performance arises from the test film only. Note that in this contact mode, we could not meaningfully test graphene films on glove material substrates, because nitrile itself has good barrier properties to DCP vapor (data not shown), making it difficult to isolate and observe the role of the graphene coating.

Fig. 7 shows the results for the direct liquid contact mode. Glove-derived nitrile rubber alone permeates DCP rapidly, having a 3 min breakthrough time followed by a rapid rise to a peak flux above 4000 × $10^{-5}$ μl-liquid per $cm^2$ min. Post-experiment inspection shows swelling and deformation of the nitrile films upon exposure to DCP (Fig. S9†). The easily measurable permeation of bare nitrile in this contact mode allows direct testing of graphene-coated nitrile samples. Pure planar GO films on nitrile extend the breakthrough time from 3 to 6 minutes, but then fail, leading to very high peak flux. Post inspection shows nitrile swelling and graphene film cracking. This evidence indicates that pure GO (1.5 μm thick) does offer some diffusional resistance, but over time sufficient DCP reaches the nitrile base layer to induce the swelling, which in turn cracks the planar (untextured) GO film leading to catastrophic failure. This catastrophic failure is not seen for pure GO on PVDF, which is a substrate that is

| Film | Thickness (um) | Breakthrough time (min) | Max. flux ($10^{-5}$ ul/cm$^2$-min) | Integrated flux, µl liquid | |
|---|---|---|---|---|---|
| | | | | after 60 min | after 480 min |
| Nitrile Rubber | 150 | 3 | 4270 | 2.31 | 11.7 |
| Pure GO on NR | 1.5 | 6 | 4910 | 2.19 | 10.9 |
| pure GO (thin) on PVDF | 5 | 31 | 753 | 0.06 | 1.58 |
| Pure GO (thick) on PVDF | 12 | 280 | 92 | 0 | 0.1 |
| GO-MC-GA on PVDF | 4.5 | no breakthrough | 0 | 0 | 0 |
| GO-MC-GA on NR (textured) | 8.7 | no breakthrough | 0 | 0 | 0 |

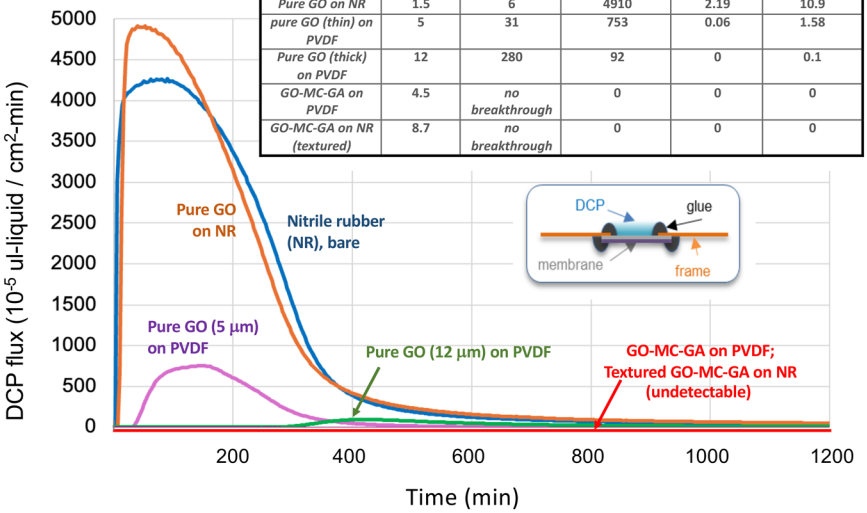


**Fig. 7** Permeation of the nerve agent simulant diethyl chlorophosphate through oven-dried graphene-based test films under conditions of direct liquid contact. The dynamic method gives DCP flux *vs.* time, and the table gives key quantitative metrics of performance. The inset shows the experimental configuration that produces direct continuous contact between the DCP liquid and top surface of the test membrane. The textured GO–MC–GA film was prepared using 50% pre-stretch. Small *Z*-offsets near the baseline were artificially introduced to enable visualization of the data for the best performing barriers.

structurally stable to DCP. These films show induction periods followed by low but measurable permeation fluxes, the thicker films of 12 µm thickness may be regarded as potentially effective barrier constructs.

The GO–MC–GA composite films are excellent barriers to DCP permeation, whether on nitrile or PVDF, and whether planar or textured. No failure is observed at any time and flux values below the detection limit through 1200 min (20 h). For these good barrier materials, a liquid DCP pool was observed to still wet the entire membrane surface after overnight testing (Fig. S9†). This confirms no loss of DCP by evaporation or migration in the system, and the presence of this residual bulk liquid is an independent confirmation of strong barrier performance. Post inspection also showed the nitrile to be intact and planar for these films (Fig. S9†), indicating that the GO–MC–GA composite coatings prevented DCP from reaching the nitrile surface in amounts necessary to induce nitrile swelling and deformation.

## Breathability

Water vapor transmission rate (WVTR) is a desirable film property in many wearable applications where sweat breathability is desirable for body heat regulation or comfort.[8,9,13] Pure graphene oxide films are known to exhibit high WVTRs,[19,28,54] and WVTR is known to decrease with GO deoxygenation.[20,54,55] The present study characterizes WVTRs for practical GO-based barrier coatings that involve binders, crosslinking, wrinkling, and imbedding.

Fig. 8 shows water vapor transmission rate defined as flux measured gravimetrically at 60 °C from a saturated water vapor source (liquid water pool) beneath film to the ambient air (see Experimental). The *Y* axis is the measured molecular flux

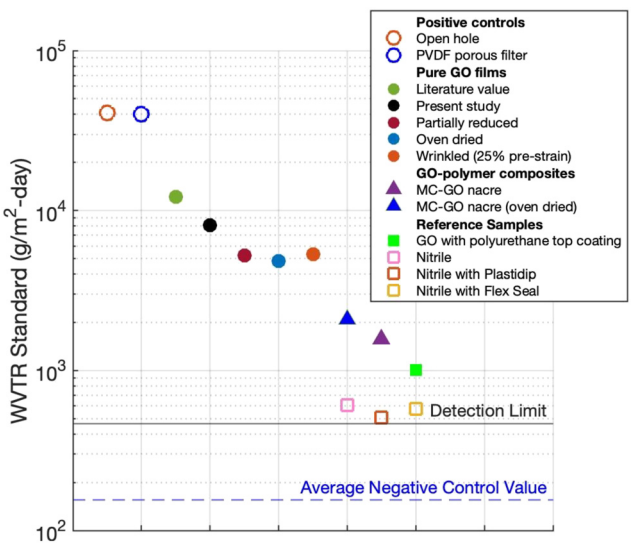


**Fig. 8** Summary of experimental water vapor transmission rates (WVTR, or breathability) obtained with the static permeation method for various pure GO films and GO–polymer composites. Data are for 37 °C and ΔRH = 90%. Positive control samples are uncovered top holes or top holes covered by a porous PVDF membrane (open circles), and negative control samples are measured with a metal foil barrier. The lower detection limit is set at 3× the negative control value. Literature data on GO film WVTR using a similar technique are from Spitz *et al.*[19] Results for pure GO films and GO composites are shown as colored circles and triangles, respectively. Glove-derived nitrile substrate barely exceeds the detection limits. The standard errors are on average ± 5% for samples far above the detection limit.

corrected to a standard RH difference, ΔRH, of 90% and with vapor pressure corrected to that at body temperature, 37 °C. The recorded WVTR of planar pure GO films equals ~9000 g $m^{-2}$ per day, which is in the range of values reported previously: 11 000 000 g $m^{-2}$ per day in ref. 19; 10 000 g $m^{-2}$ per day from Fig. 2A in Nair *et al.*[28] at 20 °C.

Andrikopoulos *et al.*[54] report 2300 g $m^{-2}$ per day using a wet cup method with lower RH driving force. The water vapor permeability is similar or slightly reduced for films subjected to partial chemical GO reduction (deoxygenation), prior oven drying (dehydration), or wrinkling. The GO–polymer composites have somewhat lower WVTRs, in the range of 1500–4000 g $m^{-2}$ per day. Nitrile rubber itself, with and without protective rubber topcoats were found to have low breathability under the same test conditions, so GO-based films coated on nitrile are not expected to add significant additional resistance to water loss.

Selected films were also characterized for WVTR by a dynamic moisture permeation method (DMPC) capable of operating in different humidity ranges. Fig. 9 shows dynamic WVTR measurements for the support materials (nitrile elastomer for solution cast films and porous PVDF substrates for the films made by vacuum filtration) and for pure GO as a function of film thickness and average humidity across the GO films. Vapor permeation through nitrile was undetectable (Fig. 9a, blue bars) even when we used a large transport area (3.6 cm diameter), used the maximum RH gradient across the film (~80–90%) achievable by this method, and increased the temperature to 60 °C to boost the transport driving force and signal. The porous PVDF support is sufficiently permeable (Fig. 9a, orange bar) to enable quantifying the breathability of the 2D layer alone with a resistance-in-series model, *i.e.* by subtracting the generally smaller contribution of the PVDF mass transfer resistance. As shown in Fig. 9b and c, pure GO films supported on PVDF filters (0.45 μm pore size) permit transport of water vapor in excess of 2000 g $m^{-2}$ per day under a relative humidity gradient of ΔRH = 50% at 30 °C. Measured breathability increases significantly with the average environmental RH the membrane is exposed to, and thus with its average hydration level, and exceeds 4000 g $m^{-2}$ per day for the 0.5 μm thick film at an average RH = 50%. The increase in WVTR at higher humidity may be due to widening of interlayer spaces. Correcting for differences in driving force ($\Delta P_{H_2O}$) between the static and dynamic methods, the two techniques show similar results for pure GO films. Assuming the driving force is linear in $\Delta P_{H_2O}$, and correcting for the temperature-dependence of water vapor pressure, the dynamic results can be scaled by $(90/50)_{\Delta RH\text{-effect}} \times (47.1/31.8)_{Pvap\text{-effect}}$ to give standard WVTRs of about 5000–10 000 g $m^{-2}$ per day, which are similar to the static results in Fig. 8. Overall, these GO-based films permeate water vapor at levels that make them attractive for wearable film applications where breathability is desired for comfort or body temperature regulation.

## Stretchability

This section characterizes the textured graphene films for extent of stretchability and discusses the implications for film design. Stiff films on soft, compliant substrates have long been known to develop out-of-plane wrinkle patterns in response to substrate shrinkage to relieve compressive stress.[56–58] Graphene on soft substrates is an ideal incompressible but flexible film, and a large body of work since 2004 has demonstrated methods to create periodic 1D wrinkles,[18,25,27,56] 2D crumple textures that are nearly isotropic,[11,18,25] or complex hierarchical textures through multiple compressive stages.[33] While the literature on graphene wrinkles and other out-of-plane textures is extensive, less is known about the stretchability of practical textured graphene-based films, including the damage-free strain limits during re-stretch, especially as a function of film thickness, composite composition, and crosslinking.

Here stretchability was characterized by video documentation during stretching and relaxation cycles (see Videos S1 and S2†). Still images extracted from those videos are shown in Fig. 10 which reveals that conventional planar (non-textured) graphene oxide films crack readily at low

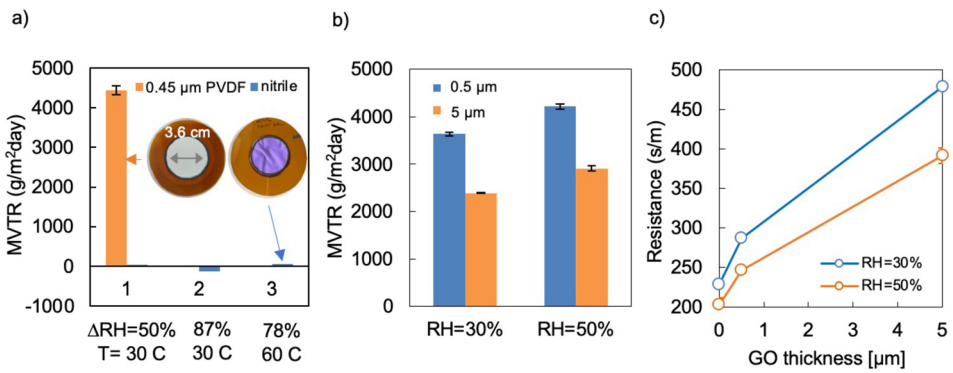


Fig. 9 Water vapor transport rates (WVTR) and derived resistances measured by a dynamic flow technique for various GO films and average humidity values. Error bars from $n \geq 2$. Most data are duplicate tests performed in tow consecutive days. a: Reference samples of nitrile glove elastomer, and the porous PVDF filter support; b and c: pure GO films of 0.5 μm and 5 μm thickness (on 0.45 μm pore size PVDF support) under a relative humidity gradient of ΔRH = 50% at 30 °C. The RH = 30% and RH = 50% labels in panel b and c indicate the average RH across the film.

 

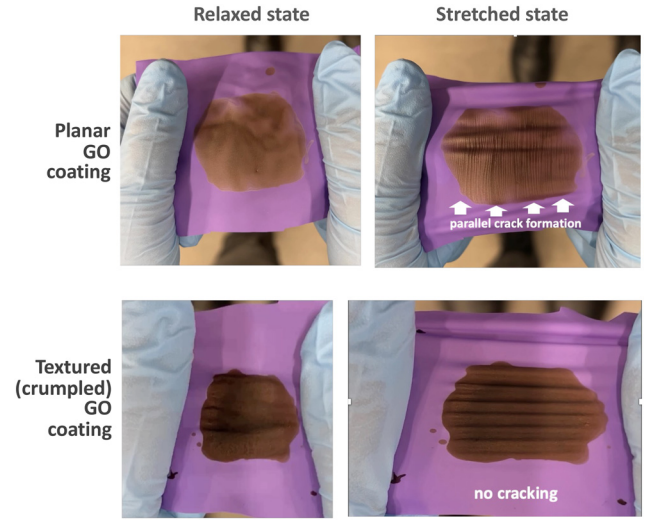


**Fig. 10** Demonstration that compressive pre-texturing of graphene oxide films renders them stretchable, with no cracks observed over multiple stretch and relax cycles. Films (0.5 μm thick) were formed by solution casting of pure graphene oxide (no polymer additive) on nitrile glove cutouts. Still images extracted from video original (see Videos S1 and S2†).

strain when the underlying nitrile substrate is stretched, while pre-textured graphene films are capable of extreme stretching without crack formation. The same sample was rotated and stretched in the *Y*-direction successfully (Fig. S10†), demonstrating that the stretchability is isotropic. This result is both desirable and expected since 2D isotropic pre-stretching was used to originally form the texture.

Fig. 11 explores the limits of crack-free stretchability in pure GO films, as a function of the extent of pre-stretch used in the fabrication process (from 33% to 100%). The plot shows that in all cases, cracking begins when re-stretch strain is equal to or slightly exceeds the pre-stretch strain. This finding suggests that the compressive folding process is fully reversible and that the GO films can withstand local stresses associated with the unfolding and re-stretching process. Zang *et al.*[25] have also reported reversible folding and unfolding, but in CVD-grown few-layer graphene on polymer substrates. Beyond the failure point, cracks become more numerous and widen (Fig. 11). The ability of graphene oxide nanosheet films to stretch can be directly controlled by the extent of pre-strain during fabrication, up to at least 100% linear strain.

Fig. 12 examines stretchability in more detail as a function of film thickness, binder addition, and extent of crosslinking. First, panel A shows the surface texture of the GO–MC–GA composite films fabricated with 50% pre-strain (left image). The textural features show a larger length scale than those for the pure GO films in this study (right image). This length scale difference can be explained using theories of stiff film buckling on compliant substrates, as follows. For small degrees of compression, the wavelength of unidirectional wrinkles, $\lambda_o$,

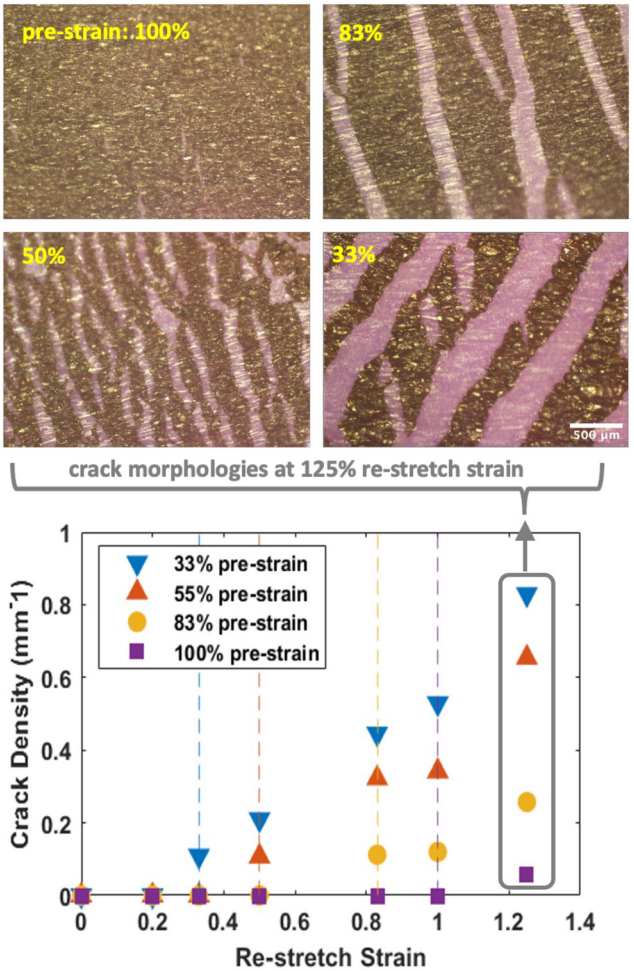


**Fig. 11** Stretchability limits for pure GO films (0.5 μm thickness) characterized by optical analysis of crack initiation and growth during stretching. Top images: examples of optical images of cracks formed on pre-stretched films after re-stretching at 125% strain. Bottom graph: crack densities for pure graphene oxide films on nitrile substrates fabricated with various pre-stain levels (33–100%) while undergoing re-stretch to and beyond the pre-stretch value. Reversible, crack-free stretchability can be achieved at linear strains up to 100%.

can be derived from perturbation theory as:

$$\lambda_0 = 2\pi h_f \left[\frac{E_f(1-\nu_s^2)}{3E_s(1-\nu_f^2)}\right]^{1/3} \quad (2)$$

where $h_f$ is the film thickness; $E_f$ and $E_s$ are the Young's moduli of film and substrate, respectively; and $\nu_s$ and $\nu_f$ are the Poisson's ratios of elastomer substrate and stiff film, respectively.[59] There is a correction to the eqn (2) prediction for large deformation,[27] but the correction is the same for all pre-strain values, so eqn (2) can be used for comparative purposes to relate lambda to film properties. For a given substrate and pre-strain, the texture length scale scales as $\lambda \sim h_f E_f^{1/3}$. The bending stiffness of a sheet scales as $h_f^3 E_f$, so $\lambda \sim$ (bending stiffness)$^{1/3}$. The GO–MC–GA films are observed to be less flexible, so the larger texture length scale is expected.

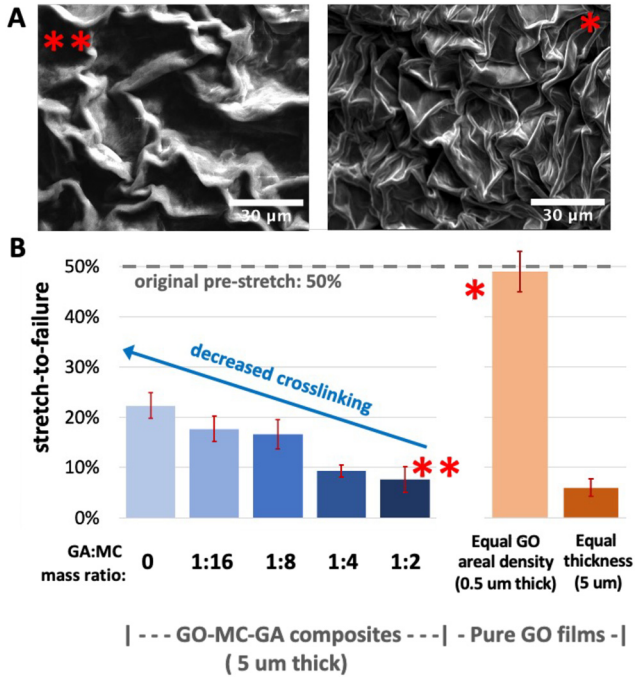


**Fig. 12** Role of binder, crosslinking and film thickness in the stretchability of textured graphene-based films. A: Textures of pure GO films (right) and GO–MC–GA composite films (left), showing different length scales of the textural features. B: Stretchability results shown as stretch-to-failure $\Delta L/L_0$ values. B-left: Reducing the concentration of the glutaraldehyde (GA) crosslinking reagent improves stretchability of the composite films. B-right: Thickness is a major variable determining the $\Delta L/L_o$ stretch-to-fail value.

Fig. 12 shows stretchability results as a function of film composition, thickness, and extent of crosslinking. The GO–MC–GA composite films with full crosslinking (**) stretch to only 10%, which is ~1/5 of the original pre-strain (50%) before failure, in contrast to the pure GO films that stretch fully. Reducing the extent of crosslinking increases stretchability up to 22% $\Delta L/L_o$. Fig. 12B also reveals that the high stretchability of pure GO films is due in part to their thinness (0.5 μm), because thick GO films (5 μm) also fail at $\Delta L/L_o$ values less than 10%. Graphene film thickness is a major variable determining stretchability, as expected from the scaling relation: bending stiffness ~$h_f^3$, which means much higher local stresses are associated with texture formation in thicker films. Overall, these studies are the first demonstration of textured graphene as a stretchable coating on glove surfaces, and show that film thickness, binder addition, and extent of crosslinking are film design parameters that can be used to tune stretchability.

### Solvent immersion stability

It is desirable that glove coatings be stable to contact with common liquid solvents, but the hydrophilic nature of GO nanosheets can make some films vulnerable to destabilization by polar liquid solvents. Solvent stability was tested by submerging the films in different polar solvents: D.I. water, ethanol, and acetone in a centrifuge tube and rotating at 65 rpm for 15 minutes. Any visible degradation, fragmentation, delamination, or redispersion of nanosheets was noted, as well as any film mass loss. The pure GO films were found to be stable in acetone, but unstable in ethanol and in water, which led to softening and visible degradation nanosheet shedding into the bulk liquid. The GO–MC–GA films and GO films with polymer topcoats were stable in all three polar solvents.

### Liquid droplet repellency

A desirable feature for some PPE applications is an outer surface that limits liquid wetting and spreading.[60–63] When PPE comes in direct contact with hazardous liquids through sprays, spills, or immersion, the surface can become contaminated with adhered liquid lenses or films that remain after use. Such residual contamination can lead to secondary exposure of the wearer, other parties, or the environment during doffing (PPE removal), handling, and disposal. Some PPE items undergo decontamination processes,[62] which become more challenging as the amount of residual toxicant increases. Surfaces that inhibit liquid wetting and spreading tend to reduce residual contamination through droplet roll off or film draining. Note that this antiwetting feature is distinct from the molecular barrier feature discussed earlier, which is designed to slow molecular transport through the PPE article to reduce primary exposure of the wearer during use.

This section explores how the biaxial textured GO platform can be formulated to minimize droplet wetting. Droplet wetting on planar graphene has been studied extensively,[25,64–66] with most studies focusing on water as the wetting liquid. Some studies have examined graphene oxide,[64–66] wrinkled pristine graphene,[25] and monolayer or few-layer graphene, where the films are so thin that the underlying substrate properties drive behavior (so-called "wetting transparency").[67] A challenge for the present work is the intrinsic chemistry of the chosen platform material, graphene oxide, which is polar and contains abundant H-bond donor and acceptor sites that favor wetting by polar liquids. Our approach is to leave the GO chemistry intact (to preserve its other advantages in aqueous processability and water vapor transport for breathability), and to treat only the outermost surface of the film with antiwetting agents. PFAS coatings are widely used to create antiwetting surfaces, but due to concerns about the environmental and health effects of PFAS,[68] our approach focuses on PFAS-free alternatives. Our scientific interest is to understand how GO texturing may synergistically enhance the antiwetting behavior of currently available chemical agents.

Fig. 13 shows the effect of various commercial PFAS-free antiwetting spray treatments (see Methods) and different degrees of compressive texturing on the contact angles of sessile liquid droplets on GO films. Two model liquids of different polarity and surface tension were selected: water

 

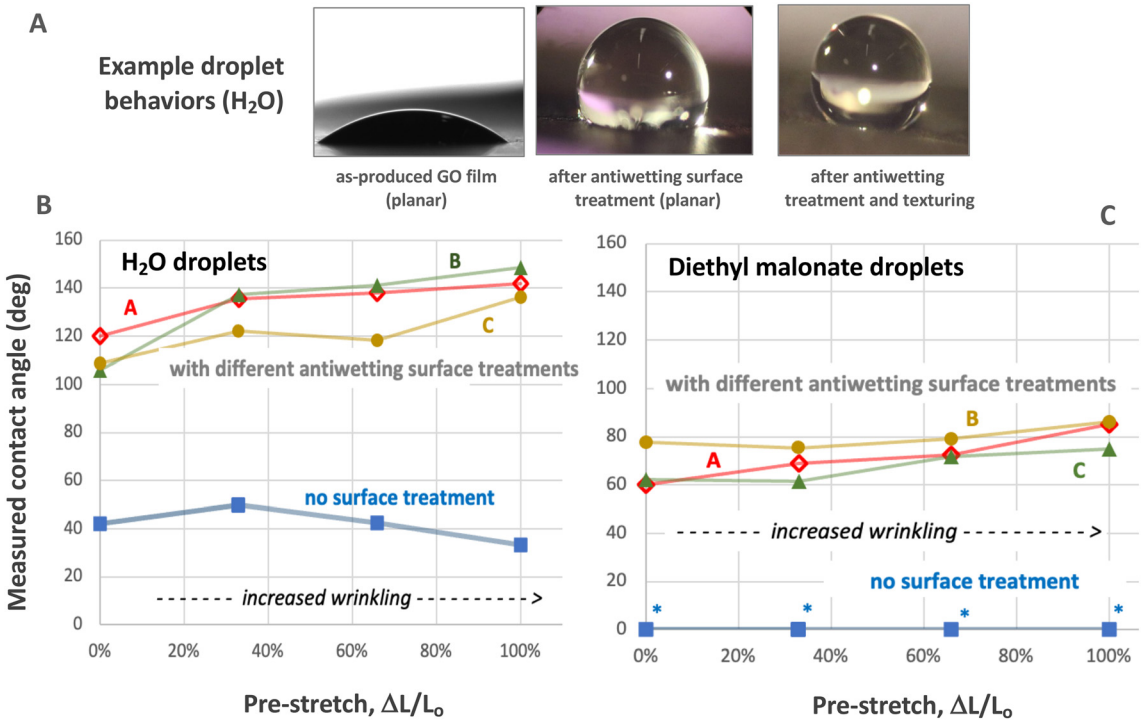


**Fig. 13** Liquid wetting of graphene-oxide-based films: effects of wrinkling (texturing) and antiwetting spray surface treatments. A: Example sessile liquid droplets showing suppression of wetting/spreading through antiwetting spray treatment (treatment C) and through the combination of the same treatment and compressive texturing (66% pre-stretch). Bottom: Quantitative data on static advancing contact angles as a function of treatment type (three antiwetting agents) and extent of compressive texturing expressed as %-pre-stretch before relaxation. B: Water; C: diethyl malonate as a polar organic compound and neurotoxicant simulant.[69] Wetting of both liquids on graphene-oxide-based films can be significantly suppressed by currently available antiwetting spray treatments and the suppression can be further enhanced by compressive film texturing. Standard errors for contact angle data (combined drop-to-drop and film-to-film) of ±3 degrees.

(72 mJ $m^{-2}$), relevant to aqueous-phase contaminants, and diethyl malonate (32 mJ $m^{-2}$), which has been recommended as a simulant for decontamination studies.[69] Fig. 13 shows the measured water contact angle on pure planar GO is 42 degrees, which in the range of values reported in the literature: 27–43 degrees.[64–66,70] High degrees of texturing cause a slight decrease in water contact angle.

Three different commercial PFAS antiwetting agents (see Materials) sprayed on the top film surface were successful at increasing water contact angle into the hydrophobic region (>90°) despite GO strong hydrophilicity. Of scientific interest here is the synergistic effect of treatment and texturing, which is a type of surface roughening (note that our "planar" films have natural wrinkle features, but these are of limited height and number and have been reported to have a negligible effect on liquid wetting[64]). Fig. 13 shows that compressive texturing enhances the liquid repellency effect with a typical increase in contact angle from 110° to 140° upon 2× linear compression (100% pre-stretch). We could not find other wetting studies on biaxial compressed, surface-treated GO, but these results are similar to the pristine graphene behavior observed by Zang *et al.*,[25] which showed a contact angle increase from ~100° to 130° upon 2× biaxial compressive texturing. The neurotoxicant simulant diethyl malonate shows very low contact angles on untreated GO, below the measurement limit, which is consistent with its lower surface tension. Antiwetting agents greatly increase these contact angles, and texturing slightly enhances the antiwetting effect.

It is interesting that texturing increases contact angle for water on hydrophobically-modified GO, decreases contact angle for water on native GO, and has only a small effect for diethyl malonate on hydrophobically-modified GO. This behavior may be explained by the Wenzel and Cassie–Baxter theories, with a transition between the two at intermediate contact angle (60–80°). Application of the Cassie–Baxter theory relies on the existence of the droplet in a suspended (Cassie) state with air or vapor pockets in the underlying solid voids.[25] This Cassie state is the equilibrium state for intrinsically poor wetting materials (here: water on modified GO) and the theory predicts that roughening will further increase the contact angle, as it does here. The Fig. 13 data for water on modified GO are consistent with the Cassie–Baxter equation: $\cos(\theta)_{observed} = f\cos(\theta)_{intrinsic} + f - 1$, for values of the solid area fraction at the interface, $f$, of about 0.4 at 100% pre-stretch. In contrast, materials with intrinsically good wetting (*e.g.* water on native GO surfaces), are typically seen in the Wenzel state, where the liquid infiltrates the porous interfacial region and in such

cases surface roughening decreases contact angle (also as seen here).

Finally, the contact angle for diethyl malonate on chemically modified but planar GO films is 60–80°, and the effect of texturing is intermediate between the two theories (no large increase or decrease).

Overall, these data show that droplet wetting and spreading on GO coatings, despite their intrinsic hydrophilicity, can be significantly suppressed using a combination of available PFAS-free antiwetting sprays and the roughening effects of compressive texturing. Highly textured films can approach the superhydrophobic regime (>140°) for aqueous droplets, which has been seen previously for pristine graphene,[25] but has not been previously demonstrated for GO-based films.

## Conclusions

This study fabricated and tested a set of graphene film formulations as ultrathin coatings on 150 μm-thick nitrile elastomeric gloves for personal chemical protection. Such coatings are required to have multiple features and functions, which depending on the specific application may include: high barrier properties for the molecular toxicant(s) of interest, ultrathin profile to preserve dexterity for handwork, stretchability, solvent contact stability, breathability (water vapor transport), and inhibition of liquid droplet wetting and spreading.

Graphene oxide coatings of <10 μm thickness were chosen for breathability and for negligible increase in glove thickness. Both static and dynamic test methods show high breathability values for these films, ranging from $10^3$–$10^4$ g-$H_2O$ $m^{-2}$ per day, which is higher than that of the nitrile base layer. Barrier behavior to volatile organic compounds was evaluated for a polar (diethyl chlorophosphate, DCP) and non-polar (hexane) model compound. Pure graphene oxide films can perform well as molecular barriers, but only in certain cases involving thicker films (~10 μm) and dry conditions. Addition of methyl cellulose as a polymeric binder followed by crosslinking with glutaraldehyde produces films with excellent barrier properties and good stability to immersion in liquid water, ethanol, and acetone.

The stretchability requirement imposed by elastomer gloves can be addressed by engineering isotropic out-of-plane texture through a fabrication sequence of 2D glove pre-stretching, film deposition, and relaxation. Some films can be fully re-stretched to the original strain used in synthesis, while other films show more limited degrees of reversible stretching without damage. The extent of damage-free stretchability is determined by film thickness, binder addition, and the extent of crosslinking (glutaraldehyde doping levels).

Liquid droplet repellency is a potential challenge for GO-based films, due to the polar, charged, and H-bonding capability of GO nanosheets. Here we demonstrate the ability to chemically modify the outermost surface of these films with commercial PFAS-free antiwetting agents, to suppress droplet wetting and spreading. Sessile drop studies on these treated surfaces show dramatic increases in contact angles for both water and diethyl malonate, and the antiwetting effect is enhanced by the out-of-plane textures, which introduce a lotus-like effect related to the increase in surface roughness.

Overall, these results suggest that textured graphene-oxide-based films can be formulated to address the multifold requirements of glove coatings. These coatings also offer the potential of green manufacturing, enabled by the selection of a non-toxic water-based polymer binder used in food applications (methylcellulose), the use of water-based deposition inks, and the selection of PFAS-free antiwetting agents. Finally, this study also sheds light on design tradeoffs that arise in applications where multiple functional requirements need to be fulfilled simultaneously. For example, binder and crosslinker addition leads to increased film stability, but can also reduce the degree of stretchability. Film thickness can often be increased to achieve a target barrier performance, but here can also increase bending stiffness and thus limit stretchability. We propose that film thickness, binder addition, and extent of crosslinking can be co-optimized for a particular application to achieve the desired balance of barrier properties, film stability, and reversible stretching range. More work is needed to characterize barrier performance for a wider range of hazardous chemicals and to relate permeabilities to molecular size, shape, polarity, and H-bond donor/acceptor sites.

## Data availability

Data for this article, including time-resolved GC-FID traces of permeant concentrations, gravimetric data on hexane and $H_2O$ permeation by the static method, FTIR spectral data for characterization, and droplet contact angle data are available in the Brown Digital Repository: **https://repository.library.brown.edu/studio/item/bdr:nwqkrwe7/**. The file will be made publicly available at the time of publication.

## Conflicts of interest

There are no conflicts to declare.

## Acknowledgements

This work was sponsored by the Department of the Defense, Defense Threat Reduction Agency, grant HDTRA1-23-1-0002 (CB11206), and by the U.S. National Science Foundation, grant CBET-2151804. The content of the information does not necessarily reflect the position or the policy of the federal government, and no official endorsement should be inferred. Work at LLNL was performed under the auspices of the US Department of Energy under contract DEAC52-07NA27344. Technical support from Zachary Saleeba at Brown is gratefully acknowledged.

 

## References

1 M. M. Falinski, R. S. Turley, J. Kidd, A. W. Lounsbury, M. Lanzarini-Lopes and A. Backhaus, *et al.*, Doing nano-enabled water treatment right: sustainability considerations from design and research through development and implementation, *Environ. Sci.: Nano*, 2020, **7**(11), 3255–3278.

2 W. Zhao, M. Adeel, P. Zhang, P. Zhou, L. Huang and Y. Zhao, *et al.*, A critical review on surface-modified nano-catalyst application for the photocatalytic degradation of volatile organic compounds, *Environ. Sci.: Nano*, 2022, **9**(1), 61–80.

3 F. Perreault, A. Fonseca De Faria and M. Elimelech, Environmental applications of graphene-based nanomaterials, *Chem. Soc. Rev.*, 2015, **44**(16), 5861–5896.

4 J. V. D. Perez, E. T. Nadres, H. N. Nguyen, M. L. P. Dalida and D. F. Rodrigues, Response surface methodology as a powerful tool to optimize the synthesis of polymer-based graphene oxide nanocomposites for simultaneous removal of cationic and anionic heavy metal contaminants, *RSC Adv.*, 2017, **7**(30), 18480–18490.

5 Y. Jiang, P. Biswas and J. D. Fortner, A review of recent developments in graphene-enabled membranes for water treatment, *Environ. Sci.: Water Res. Technol.*, 2016, **2**(6), 915–922.

6 M. S. Mauter, I. Zucker, F. Perreault, J. R. Werber, J. H. Kim and M. Elimelech, The role of nanotechnology in tackling global water challenges, *Nat. Sustain.*, 2018, **1**(4), 166–175.

7 T. Zhang, G. V. Lowry, N. L. Capiro, J. Chen, W. Chen and Y. Chen, *et al.*, In situ remediation of subsurface contamination: opportunities and challenges for nanotechnology and advanced materials, *Environ. Sci.: Nano*, 2019, **6**(5), 1283–1302.

8 S. Bhattacharjee, R. Joshi, A. A. Chughtai and C. R. Macintyre, Graphene Modified Multifunctional Personal Protective Clothing, *Adv. Mater. Interfaces*, 2019, **6**(21), 1900622.

9 K. Ma, Y. H. Cheung, K. O. Kirlikovali, X. Wang, T. Islamoglu and J. H. Xin, *et al.*, Protection against Chemical Warfare Agents and Biological Threats Using Metal–Organic Frameworks as Active Layers, *Acc. Mater. Res.*, 2023, **4**(2), 168–179.

10 C. Peng, Z. Iqbal, K. K. Sirkar and G. W. Peterson, Graphene Oxide-Based Membrane as a Protective Barrier against Toxic Vapors and Gases, *ACS Appl. Mater. Interfaces*, 2020, **12**(9), 11094–11103.

11 P. Y. Chen, M. Zhang, M. Liu, I. Y. Wong and R. H. Hurt, Ultra-Stretchable Graphene-Based Molecular Barriers for Chemical Protection, Detection, and Actuation, *ACS Nano*, 2017, **12**(1), 234.

12 Y. Kim, M. Choi, J. Heo, S. Jung, D. Ka and H. Lee, *et al.*, Blocking chemical warfare agent simulants by graphene oxide/polymer multilayer membrane based on hydrogen bonding and size sieving effect, *J. Hazard. Mater.*, 2022, **427**, 127884.

13 Y. Song, C. Peng, Z. Iqbal, K. K. Sirkar, G. W. Peterson and J. J. Mahle, *et al.*, Graphene Oxide and Metal-Organic Framework-Based Breathable Barrier Membranes for Toxic Vapors, *ACS Appl. Mater. Interfaces*, 2022, **14**(27), 31321–31331.

14 K. Ma, M. C. Wasson, X. Wang, X. Zhang, K. B. Idrees and Z. Chen, *et al.*, Near-instantaneous catalytic hydrolysis of organophosphorus nerve agents with zirconium-based MOF/hydrogel composites, *Chem Catal.*, 2021, **1**(3), 721–733.

15 C. K. Bensel, The effects of various thicknesses of chemical protective gloves on manual dexterity, *Ergonomics*, 1993, **36**(6), 687–696.

16 P. Mylon, M. J. Carré, N. Martin and R. Lewis, How do gloves affect cutaneous sensibility in medical practice? Two new applied tests, *Proc. Inst. Mech. Eng., Part H*, 2017, **231**(1), 28–39.

17 J. S. Bunch, S. S. Verbridge, J. S. Alden, A. M. van der Zande, J. M. Parpia and H. G. Craighead, *et al.*, Impermeable Atomic Membranes from Graphene Sheets, *Nano Lett.*, 2008, **8**(8), 2458–2462.

18 V. Berry, Impermeability of graphene and its applications, *Carbon*, 2013, **62**, 1–10.

19 R. Spitz Steinberg, M. Cruz, N. G. A. Mahfouz, Y. Qiu and R. H. Hurt, Breathable Vapor Toxicant Barriers Based on Multilayer Graphene Oxide, *ACS Nano*, 2017, **11**(6), 5670–5679.

20 Y. Su, V. G. Kravets, S. L. Wong, J. Waters, A. K. Geim and R. R. Nair, Impermeable barrier films and protective coatings based on reduced graphene oxide, *Nat. Commun.*, 2014, **5**(1), 4843.

21 R. K. Layek, K. R. Ramakrishnan, E. Sarlin, O. Orell, M. Kanerva and J. Vuorinen, *et al.*, Layered structure graphene oxide/methylcellulose composites with enhanced mechanical and gas barrier properties, *J. Mater. Chem. A*, 2018, **6**(27), 13203–13214.

22 R. K. Joshi, P. Carbone, F. C. Wang, V. G. Kravets, Y. Su and I. V. Grigorieva, *et al.*, Precise and ultrafast molecular sieving through graphene oxide membranes, *Science*, 2014, **343**(6172), 752–754.

23 S. Zheng, Q. Tu, J. J. Urban, S. Li and B. Mi, Swelling of Graphene Oxide Membranes in Aqueous Solution: Characterization of Interlayer Spacing and Insight into Water Transport Mechanisms, *ACS Nano*, 2017, **11**(6), 6440–6450.

24 A. Iakunkov and A. V. Talyzin, Swelling properties of graphite oxides and graphene oxide multilayered materials, *Nanoscale*, 2020, **12**(41), 21060–21093.

25 J. Zang, S. Ryu, N. Pugno, Q. Wang, Q. Tu and M. J. Buehler, *et al.*, Multifunctionality and control of the crumpling and unfolding of large-area graphene, *Nat. Mater.*, 2013, **12**(4), 321–325.

26 S. Deng and V. Berry, Wrinkled, rippled and crumpled graphene: an overview of formation mechanism, electronic properties, and applications, *Mater. Today*, 2016, **19**(4), 197–212.

27 Z. Wang, D. Tonderys, S. E. Leggett, E. K. Williams, M. T. Kiani and R. S. Steinberg, *et al.*, Wrinkled, wavelength-tunable graphene-based surface topographies for directing cell alignment and morphology, *Carbon*, 2016, **97**, 14.

28 R. R. Nair, H. A. Wu, P. N. Jayaram, I. V. Grigorieva and A. K. Geim, Unimpeded Permeation of Water Through Helium-Leak–Tight Graphene-Based Membranes, *Science*, 2012, **335**(6067), 442–444.
29 M. Liu, P. J. Weston and R. H. Hurt, Controlling nanochannel orientation and dimensions in graphene-based nanofluidic membranes, *Nat. Commun.*, 2021, **12**(1), 507.
30 M. Liu, D. C. C. Fernandes, Z. S. S. L. Saleeba and R. H. Hurt, Controlled Release of Molecular Intercalants from Two-Dimensional Nanosheet Films, *ACS Nano*, 2021, **15**(12), 20105–20115.
31 D. Lozano-Castelló, D. Cazorla-Amorós and A. Linares-Solano, Usefulness of CO2 adsorption at 273 K for the characterization of porous carbons, *Carbon*, 2004, **42**(7), 1233–1242.
32 Y. Kwon, M. Liu, C. Castilho, Z. Saleeba, R. Hurt and I. Külaots, Controlling pore structure and conductivity in graphene nanosheet films through partial thermal exfoliation, *Carbon*, 2020, **174**, 227.
33 P. Y. Chen, J. Sodhi, Y. Qiu, T. M. Valentin, R. S. Steinberg and Z. Wang, *et al.*, Multiscale Graphene Topographies Programmed by Sequential Mechanical Deformation, *Adv. Mater.*, 2016, **28**(18), 3564–3571.
34 P. W. Gibson and H. L. Schreuder-Gibson, Influence of Hydration State on Permeation Testing and Vapor Transport Properties of Protective Clothing Layers, *J. Eng. Fibers Fabr.*, 2009, **4**(4), 155892500900400409.
35 N. Bui, E. R. Meshot, S. Kim, J. Peña, P. W. Gibson and K. J. Wu, *et al.*, Ultrabreathable and Protective Membranes with Sub-5 nm Carbon Nanotube Pores, *Adv. Mater.*, 2016, **28**(28), 5871–5877.
36 Y. Li, C. Chen, E. Meshot, S. Buchsbaum, M. Herbert and R. Zhu, *et al.*, Autonomously Responsive Membranes for Chemical Warfare Protection, *Adv. Funct. Mater.*, 2020, **30**, 2000258.
37 C. J. Castilho, D. Li, M. Liu, Y. Liu, H. Gao and R. H. Hurt, Mosquito bite prevention through graphene barrier layers, *Proc. Natl. Acad. Sci. U. S. A.*, 2019, **116**(37), 18304.
38 A. P. Samanta, M. S. Ali, J. T. Orasugh, S. K. Ghosh and D. Chattopadhyay, Crosslinked nanocollagen-cellulose nanofibrils reinforced electrospun polyvinyl alcohol/methylcellulose/polyethylene glycol bionanocomposites: Study of material properties and sustained release of ketorolac tromethamine, *Carbohydr. Polym. Technol. Appl.*, 2022, **3**, 100195.
39 S. Park, D. A. Dikin, S. T. Nguyen and R. S. Ruoff, Graphene Oxide Sheets Chemically Cross-Linked by Polyallylamine, *J. Phys. Chem. C*, 2009, **113**(36), 15801–15804.
40 Z. Zhao, Q. Li, J. Gong, Z. Li and J. Zhang, Hybrid poly(allylamine hydrochloride)–graphene oxide microcapsules: preparation, characterization and application in textiles with controlled release behavior, *Mater. Adv.*, 2020, **1**(4), 804–813.
41 E. N. Mohamed, A. I. Abd-Elhamid, A. A. El-Bardan, H. M. A. Soliman and M. S. Mohy-Eldin, Development of carboxymethyl cellulose-graphene oxide biobased composite for the removal of methylene blue cationic dye model contaminate from wastewater, *Sci. Rep.*, 2023, **13**(1), 14265.
42 A. Satti, P. Larpent and Y. Gun'ko, Improvement of mechanical properties of graphene oxide/poly(allylamine) composites by chemical crosslinking, *Carbon*, 2010, **48**, 3376–3381.
43 Z. Zhang, T. Guan, X. Zhang, L. Shen and N. Bao, High-Strength-Reduced Graphene Oxide/Carboxymethyl Cellulose Composite Fibers for High-Performance Flexible Supercapacitors, *Ind. Eng. Chem. Res.*, 2021, **60**(24), 8753–8761.
44 S. Wan, J. Peng, Y. Li, H. Hu, L. Jiang and Q. Cheng, Use of synergistic interactions to fabricate strong, tough, and conductive artificial nacre based on graphene oxide and chitosan, *ACS Nano*, 2015, **9**(10), 9830–9836.
45 S. Mohammed, H. M. Hegab and R. Ou, Nanofiltration performance of glutaraldehyde crosslinked graphene oxide-cellulose nanofiber membrane, *Chem. Eng. Res. Des.*, 2022, **183**, 1–12.
46 S. Rimdusit, K. Somsaeng, P. Kewsuwan, C. Jubsilp and S. Tiptipakorn, Comparison of Gamma Radiation Crosslinking and Chemical Crosslinking on Properties of Methylcellulose Hydrogel, *Eng. J.*, 2012, **16**, 15–28.
47 W. Treesuppharat, P. Rojanapanthu, C. Siangsanoh, H. Manuspiya and S. Ummartyotin, Synthesis and characterization of bacterial cellulose and gelatin-based hydrogel composites for drug-delivery systems, *Biotechnol. Rep.*, 2017, **15**, 84–91.
48 M. Dahanayaka and J. W. Chew, Organic Solvent Permeation through Negatively Charged Graphene Oxide Membranes, *ACS Sustainable Chem. Eng.*, 2022, **10**(4), 1499–1508.
49 L. Huang, Y. Li, Q. Zhou, W. Yuan and G. Shi, Graphene Oxide Membranes with Tunable Semipermeability in Organic Solvents, *Adv. Mater.*, 2015, **27**(25), 3797–3802.
50 L. Zheng, S. Jerrams, Z. Xu, L. Zhang, L. Liu and S. Wen, Enhanced gas barrier properties of graphene oxide/rubber composites with strong interfaces constructed by graphene oxide and sulfur, *Chem. Eng. J.*, 2020, **383**, 123100.
51 M. D. Ong, I. Vasquez, B. Alvarez, D. R. Cho, M. B. Williams and D. Vincent, *et al.*, Modification of Cellulose Acetate Microfiltration Membranes Using Graphene Oxide-Polyethyleneimine for Enhanced Dye Rejection, *Membranes*, 2023, **13**(2), 143.
52 H. Qu, A. Rayabharam, X. Wu, P. Wang, Y. Li and J. Fagan, *et al.*, Selective filling of n-hexane in a tight nanopore, *Nat. Commun.*, 2021, **12**(1), 310.
53 B. Rezania, N. Severin, A. V. Talyzin and J. P. Rabe, Hydration of Bilayered Graphene Oxide, *Nano Lett.*, 2014, **14**(7), 3993–3998.
54 K. S. Andrikopoulos, G. Bounos, D. Tasis, L. Sygellou, V. Drakopoulos and G. A. Voyiatzis, The Effect of Thermal Reduction on the Water Vapor Permeation in Graphene Oxide Membranes, *Adv. Mater. Interfaces*, 2014, **1**(8), 1400250.
55 C. A. Amadei, A. Montessori, J. P. Kadow, S. Succi and C. D. Vecitis, Role of Oxygen Functionalities in Graphene Oxide

 

Architectural Laminate Subnanometer Spacing and Water Transport, *Environ. Sci. Technol.*, 2017, **51**(8), 4280–4288.
56 M. A. Biot and G. I. Taylor, Folding instability of a layered viscoelastic medium under compression, *Proc. R. Soc. London, Ser. A*, 1997, **242**(1231), 444–454.
57 N. Bowden, S. Brittain, A. G. Evans, J. W. Hutchinson and G. M. Whitesides, Spontaneous formation of ordered structures in thin films of metals supported on an elastomeric polymer, *Nature*, 1998, **393**(6681), 146–149.
58 J. Genzer and J. Groenewold, Soft matter with hard skin: From skin wrinkles to templating and material characterization, *Soft Matter*, 2006, **2**(4), 310–323.
59 D. A. Kunz, P. Feicht, S. Gödrich, H. Thurn, G. Papastavrou and A. Fery, *et al.*, Space-Resolved In-Plane Moduli of Graphene Oxide and Chemically Derived Graphene Applying a Simple Wrinkling Procedure, *Adv. Mater.*, 2013, **25**(9), 1337–1341.
60 N. Atthi, O. Nimittrakoolchai, W. Jeamsaksiri and S. Supothina, Chemical Resistant Improvement of Natural Rubber and Nitrile Gloves by Coating with Hydrophobic Film, *Adv. Mater. Res.*, 2008, **55–57**, 741–744.
61 E. Irzmańska, A. Jastrzębska and M. Makowicz, Preliminary Research: Validation of the Method of Evaluating Resistance to Surface Wetting with Liquid of Protective Materials Intended for Polymer Protective Gloves, *Int. J. Environ. Res. Public Health*, 2021, **18**(17), 9202.
62 W. Li, Y. Wang, X. Tang, T. T. T. Yuen, X. Han and J. Li, *et al.*, Liquid repellency enabled antipathogen coatings, *Mater. Today Bio*, 2021, **12**, 100145.
63 L. Oudejans, J. O'Kelly, A. S. Evans, B. Wyrzykowska-Ceradini, A. Touati and D. Tabor, *et al.*, Decontamination of personal protective equipment and related materials contaminated with toxic industrial chemicals and chemical warfare agent surrogates, *J. Environ. Chem. Eng.*, 2016, **4**(3), 2745–2753.
64 F. Perrozzi, S. Croce, E. Treossi, V. Palermo, S. Santucci and G. Fioravanti, *et al.*, Reduction dependent wetting properties of graphene oxide, *Carbon*, 2014, **77**, 473–480.
65 N. Wei, C. Lv and Z. Xu, Wetting of Graphene Oxide: A Molecular Dynamics Study, *Langmuir*, 2014, **30**(12), 3572–3578.
66 J. Kim, W. H. Khoh, B. H. Wee and J. D. Hong, Fabrication of flexible reduced graphene oxide–TiO2 freestanding films for supercapacitor application, *RSC Adv.*, 2015, **5**(13), 9904–9911.
67 J. Rafiee, X. Mi, H. Gullapalli, A. V. Thomas, F. Yavari and Y. Shi, *et al.*, Wetting transparency of graphene, *Nat. Mater.*, 2012, **11**(3), 217–222.
68 S. E. Fenton, A. Ducatman, A. Boobis, J. C. DeWitt, C. Lau and C. Ng, *et al.*, Per- and Polyfluoroalkyl Substance Toxicity and Human Health Review: Current State of Knowledge and Strategies for Informing Future Research, *Environ. Toxicol. Chem.*, 2021, **40**(3), 606–630.
69 T. James, S. Wyke, T. Marczylo, S. Collins, T. Gaulton and K. Foxall, *et al.*, Chemical warfare agent simulants for human volunteer trials of emergency decontamination: A systematic review, *J. Appl. Toxicol.*, 2017, **38**(1), 113.
70 D. Kang, S. H. Kim, D. Shin, J. T. Oh, M. G. Kim and P. C. Lee, Hygroscopic Behavior of Polypropylene Nanocomposites Filled with Graphene Functionalized by Alkylated Chains, *Nanomaterials*, 2022, **12**(23), 4130.